International Journal of Nanomedicine

Dovepress
open access to scientific and medical research

Open Access Full Text Article

ORIGINAL RESEARCH

# Construction of CXCR4 Receptor-Targeted $CuFeSe_2$ Nano Theranostic Platform and Its Application in MR/CT Dual Model Imaging and Photothermal Therapy

Wenlu Li[1,2,*], Yaolin Gong[1,2,*], Jing Zhang[1,2], Jiong Liu[1,2], Jiali Li[1,2], Shaozhi Fu[3], Wen Xiu Ren[1,2], Jian Shu[1,2]

[1]Department of Radiology, The Affiliated Hospital of Southwest Medical University, Luzhou, Sichuan, People's Republic of China; [2]Nuclear Medicine and Molecular Imaging Key Laboratory of Sichuan Province, The Affiliated Hospital of Southwest Medical University, Luzhou, Sichuan, People's Republic of China; [3]Department of Oncology, The Affiliated Hospital of Southwest Medical University, Luzhou, Sichuan, People's Republic of China

*These authors contributed equally to this work

Correspondence: Wen Xiu Ren; Jian Shu, Department of Radiology, The Affiliated Hospital of Southwest Medical University, No. 25 Taiping St, Jiangyang District, Luzhou, Sichuan, 646000, People's Republic of China, Email xrenwenxiux@swmu.edu.cn; shujiannc@swmu.edu.cn



**Introduction:** Targeting, imaging, and treating tumors represent major clinical challenges. Developing effective theranostic agents to address these issues is an urgent need.

**Methods:** We introduce an "all-in-one" tumor-targeted theranostic platform using $CuFeSe_2$-based composite nanoparticles ($CuFeSe_2$@PA) for magnetic resonance (MR) and computed tomography (CT) dual model imaging-guided hyperthermia tumor ablation. Plerixafor (AMD3100) is bonded to the surface of $CuFeSe_2$ as a targeting unit. Due to the robust interaction between AMD3100 and the overexpressed Chemokine CXC type receptor 4 (CXCR4) on the membrane of 4T1 cancer cells, $CuFeSe_2$@PA specifically recognizes 4T1 cancer cells, enriching the tumor region.

**Results:** $CuFeSe_2$@PA serves as a contrast agent for $T_2$-weighted MR imaging (relaxivity value of 1.61 $mM^{-1}$ $s^{-1}$) and CT imaging. Moreover, it effectively suppresses tumor growth through photothermal therapy (PTT) owing to its high photothermal conversion capability and stability, with minimized side effects demonstrated both in vitro and in vivo.

**Discussion:** $CuFeSe_2$@PA nanoparticles show potential as dual-mode imaging contrast agents for MR and CT and provide an effective means of tumor treatment through photothermal therapy. The surface modification with Plerixafor enhances the targeting ability of the nanoparticles, performing more significant efficacy and biocompatibility in the 4T1 cancer cell model. The study demonstrates that $CuFeSe_2$@PA is a promising multifunctional theranostic platform with clinical application potential.

**Keywords:** tumor targeting, photothermal therapy, dual model imaging, theranostic platform, chemokine cxc type receptor 4

## Introduction

The complexity and rapid development of cancer renders it the second greatest threat to human health worldwide.[1] Current clinical approaches to cancer treatment typically involve a combination of surgery, chemotherapy, and radiotherapy. However, surgical treatment may pose challenges such as residual incisal margins, postoperative recurrence, or metastasis. Furthermore, the non-selectivity of radiotherapy and chemotherapy can lead to damage to normal cells and tissues. In addition, chemotherapy is susceptible to drug resistance, resulting in diminished efficacy.[2] Photothermal therapy (PTT), an emerging and multidisciplinary strategy for tumor therapy, presents distinct advantages, including minimal invasiveness, high efficiency, few side effects, and repeatability.[3] PTT is beneficial for preserving the quality of life for patients and is considered a potential alternative to traditional clinical cancer treatments. However, despite its potential, many reported PTT materials are delivered to living systems in a non-active targeting manner, which severely

Received: 4 July 2024
Accepted: 3 September 2024
Published: 7 September 2024

**Graphical Abstract**

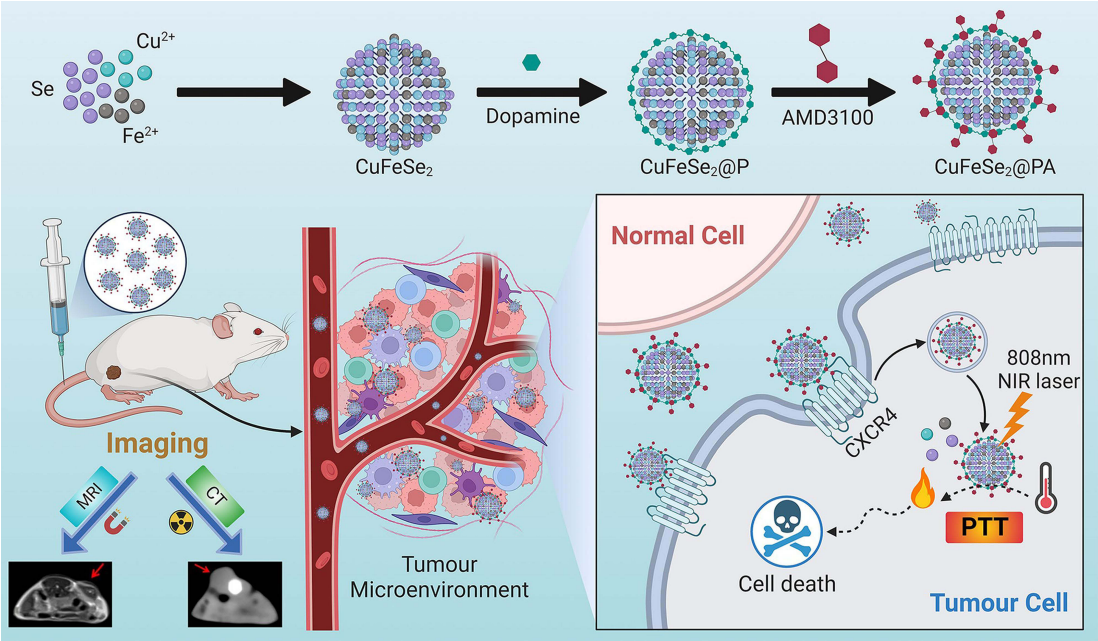


restricts their clinical applications.[4–6] Consequently, the development of PTT materials that can locate tumor regions with active targeting functions and simultaneously eradicate tumor cells remains a significant challenge.

Early diagnosis is another key aspect of cancer treatment as evidenced by significantly improved 5-year survival rates and prognoses of patients diagnosed in the early stages. In clinical practice, magnetic resonance (MR) imaging emerges as a non-invasive diagnostic method offering exceptional soft tissue contrast, along with anatomical and metabolic function information without ionizing radiation and depth limitations of the lesion.[7] However, its limitation lies in low sensitivity. Computed tomography (CT) has advantages in spatial resolution, image clarity, and scanning time but exhibits poor soft-tissue contrast. The dual-modality imaging mode of CT combined with MR can compensate for the limitations of both, amplify the advantages of each, and more comprehensively reflect the imaging information of tumors. Given the challenges in early diagnosis, the lack of precision of personalized treatment, and prognostic evaluation of tumors, significant attention has shifted towards nanomaterials for the integration of diagnosis and therapy.[1] These nanotheranostic platforms hold great promise in cancer diagnosis and treatment.[8,9]

Recently, the photoelectric properties of I–III–VI2 ternary sulfur semiconductor materials have shown broad application prospects in solar cells, photodetectors, biological imaging probes, and electrothermal equipment.[10] Notably, copper (Cu) characterized by a high atomic number, is adept at absorbing X-rays for CT imaging. Iron (Fe) exhibiting superparamagnetism, serves as a negative contrast agent in $T_2$-weighted MRI sequences. Selenium (Se) can be used to improve the PTT efficiency of nanoparticles.[11] Therefore, $CuFeSe_2$ nanoparticle emerged as a promising theranostic material. Jiang et al[12] demonstrated the excellent photothermal anti-tumor functionality of $CuFeSe_2$ under near-infrared laser irradiation. Some studies have used methoxy-polyethylene glycol polycaprolactone[13] and folic acid[14] to modify the surface of $CuFeSe_2$ for favorable in vivo and in vitro MR-CT dual-modal imaging performance. In addition, Liu et al[15] loaded doxorubicin onto $CuFeSe_2$ nanosheets to achieve synergistic chemotherapy and PTT at the cellular level. However, there have been few reports on the application of tumor-targeted $CuFeSe_2$ in MR-CT dual-modal imaging and PTT. Therefore, it is necessary to combine $CuFeSe_2$ with targeted ligands to fully exploit its diagnostic and therapeutic functions.

Chemokines are proteins belonging to the cytokine superfamily with a molecular weight of approximately 8–10 KDa. Initially, identified for their role in regulating the transport of white blood cells throughout the body,[16] chemokines are recognized for their function in promoting and directing cell migration and regulating homeostasis. Chemokine CXC type ligand-12 (CXCL12) is a steady-state chemokine that controls hematopoietic cell transport and lymphoid tissue structure. After binding to the Chemokine CXC type receptor 4 (CXCR4), it plays an important role in cell proliferation, migration, and adhesion by activating downstream effector proteins and cell signaling pathways. Studies have shown that CXCL12 can maintain tumor survival and promote tumor metastasis and spread.[17,18] CXCR4 is highly expressed on the surface of various malignant tumors, such as breast cancer, ovarian cancer, and pancreatic cancer, making it a potential target for tumor imaging and treatment.[19]

Plerixafor (also known as AMD3100), the first non-peptide CXCR4-specific antagonist in clinical trials, is a tetraazacyclotetradecane drug approved by the United States Food and Drug Administration. In clinical practice, AMD3100 can be used to treat non-Hodgkin lymphoma and multiple myeloma, and its primary mechanism is to block the binding of CXCR4 and its homologous ligand CXCL12.[20] Owing to the special interaction between AMD3100 and CXCR4, AMD3100 can be modified with radioisotopes of transition metal elements, facilitating targeted tumor imaging.[21] Some studies have shown that AMD3100 labeled with $^{64}Cu$[22] can be used for positron emission tomography (PET) monitoring of 4T1 breast cancer in situ models. Moreover, $^{99}$mTc labeled AMD3100[23] can be served as a single-photon emission computed tomography (SPECT) imaging tracer for prostate cancer models. Miao et al[24] used AMD3100-modified nanoplatforms modified nano platforms to successfully monitor the development of a 4T1 breast cancer model and lung metastasis using MR.

Building on the above theories, an "all-in-one" tumor-targeted theranostic platform of $CuFeSe_2$-based composite nanoparticle ($CuFeSe_2$@PA) has been developed for MR and CT dual model imaging-guided PTT of cancer. The construction of $CuFeSe_2$@PA can be divided into two stages. First, polydopamine (PDA) was modified on the surface of $CuFeSe_2$ by the oxidative self-polymerization of dopamine hydrochloride in an alkaline environment.[25] This process results in the formation of $CuFeSe_2$@P nanoparticles. By minimizing direct contact with the biological environment, PDA generates a protective covering that improves biocompatibility and reduces toxicity.[26] Additionally, it offers reactive areas for additional functionalization with medications or biomolecules.[27,28] Additionally, the PDA layer's stability under physiological conditions prolongs nanoparticle circulation time and improves stability in vivo.[29] Next, PEG-modified AMD3100 was linked to the surface of $CuFeSe_2$@P by nucleophilic addition to enhance the tumor-targeting performance. Subsequently, MR/CT dual-model imaging and PTT properties of $CuFeSe_2$@PA were systematically investigated. The results showed that the $CuFeSe_2$@PA theranostic platform could specifically recognize 4T1 cancer cells and enrich the tumor region while exhibiting excellent MR/CT imaging ability and photothermal performance. This could effectively induce MR/CT imaging-guided hyperthermia tumor ablation in vitro and in vivo. All of these characteristics of the $CuFeSe_2$@PA platform point to its potential for accurate and powerful cancer theranostics, providing a viable path forward for sophisticated clinical applications.

# Materials and Methods

## Materials

Selenium powder (Se, ≥99.5%), sodium borohydride ($NaBH_4$, ≥99%), copper(II) chloride dihydrate ($CuCl_2{\cdot}2H_2O$), ferrous sulfate heptahydrate ($FeSO_4{\cdot}7H_2O$), Roswell Park Memorial Institute-1640 (RPMI-1640) medium, Dulbecco's minimum essential medium (DMEM), high sugar medium, and fetal bovine serum (FBS) were purchased from Sigma-Aldrich (USA). Plerixafor (AMD3100) and Dopamine (DA) were purchased from Aladdin (Shanghai, China). N-hydroxysuccinimide-polyethylene glycol-maleimide imide (NHS-PEG-Mal) was purchased from JenKem (Beijing, China). Phosphate buffer (PBS, pH 7.2–7.4), sodium borate buffer ($Na_2B_4O_7$, pH8.5), Tris hydrochloride buffer (Tris, pH8.5), and penicillin-streptomycin solution were purchased from Beyotime (Shanghai, China). All reagents were used as received without further purification.

## Synthetic Procedures

### Synthesis of $CuFeSe_2$

$CuFeSe_2$ was prepared according to a previously reported method.[13,14] First, 160.5 mg Se powder and 158.4 mg $NaBH_4$ were dispersed into a two-neck flask filled with 100 mL of deionized water and stirred magnetically for 1 h under $N_2$ protection. The color of the solution gradually changed from dark gray to colorless. Next, 279.5 mg $FeSO_4.7H_2O$ and 172.5 mg $CuCl_2.2H_2O$ were dissolved in 5 mL of deionized water and then quickly added to the flask. The reaction mixture was then stirred at room temperature for 2 h. When the reaction was complete, the mixture was washed (deionized water) and centrifuged (9000 rpm, 15 min) three times to obtain $CuFeSe_2$.

### Synthesis of $CuFeSe_2$@P

400 mg DA and 200 mg synthesized $CuFeSe_2$ were dispersed in 100 mL of tris buffer solution (pH 8.5) and stirred at room temperature in the dark for 8 h. After the reaction was complete, the mixture was washed (deionized water) and centrifuged (9000 rpm, 15 min) three times to obtain a $CuFeSe_2$@P precipitate. The precipitate was freeze-dried for standard application.

### Synthesis of $CuFeSe_2$@PA

First, 50 mg NHS-PEG-Mal and 20 mg AMD3100 were dissolved in 4 mL mixed media of methanol and water (7/3, v/v). After stirring at 37 °C for 48 h, the reaction was continued at 50 °C for another 24 h. Then, the obtained solution was dialyzed for 24 h using a dialysis bag (1Kd) and deionized water. Deionized water was replaced at specific intervals during this process. PEG-AMD was obtained by freeze-drying the dialyzed solution. The structure of the PEG-AMD was confirmed by 1H NMR analysis (Figure S1 and S2). Finally, 35 mg of PEG-AMD and 70 mg of $CuFeSe_2$@P were dispersed in 60 mL of sodium borate buffer (pH 8.5) for 1.5 h in the dark and centrifuged (9000 rpm, 15 min) three times to obtain the $CuFeSe_2$@PA precipitate. The precipitate was freeze-dried for standard application.

### Synthesis of $CuFeSe_2$@PA-Cy5.5 and $CuFeSe_2$@P-Cy5.5

On completion of the synthesis of $CuFeSe_2$@PA, 50 μL Cy5.5-NHS (10 mg/mL) was added to the solution and the reaction was continued in the dark for another 0.5 h. The dispersion was centrifuged at 9000 rpm for 15 min. The supernatant was removed, and the precipitate was freeze-dried to get $CuFeSe_2$@PA-Cy5.5. $CuFeSe_2$@P-Cy5.5 was synthesized following the same procedure.

## Characterization

Transmission electron microscopy (TEM, FEI, USA) was employed to capture images and record morphologies of $CuFeSe_2$ and $CuFeSe_2$@PA, and Nano Measure was utilized to measure their sizes. Cobalt target wide-angle diffraction testing was performed on $CuFeSe_2$, $CuFeSe_2$@P, and $CuFeSe_2$@PA using an X-ray powder diffractometer (XRD; Bruker, Germany), and their crystal structures were characterized. The contents and proportions of Cu, Fe, and Se in $CuFeSe_2$, $CuFeSe_2$@P, and $CuFeSe_2$@PA were measured by inductively coupled plasma optical emission spectroscopy (ICP-OES, Agilent, USA). Fourier transform infrared (FTIR, Nicolet, USA) and $^1H$ nuclear magnetic resonance (NMR, Bruker, Germany) spectroscopy were used to confirm the presence of $CuFeSe_2$@PA.

## Hemolysis of $CuFeSe_2$@PA

Blood was extracted from nude mice via the orbital veins,[30] and subsequent to centrifugation (4000 rpm, 10 min), red blood cells were obtained and subsequently washed with saline. The erythrocytes were then diluted to a concentration of 2% using normal saline. Subsequently, varying concentrations of $CuFeSe_2$@PA solutions were added to the erythrocytes, thoroughly mixed, and incubated at 37°C for 2 hours. Following the completion of the incubation period, centrifugation (4000 rpm, 10 min) was performed, and the color of the supernatant was observed and documented. The supernatant, with a volume of 100 μL per well, was placed in a 96-well plate. Utilizing a multiplate reader (Cyation5, BioTek, America), the absorbance of the supernatant at 540 nm was determined, allowing for the calculation of the hemolysis rate. The positive control group underwent treatment with pure water, while the negative control group was treated with normal saline.

## Photothermal Performance of $CuFeSe_2$@PA

The photothermal performance of $CuFeSe_2$@PA was assessed by irradiating a 1 mL dispersion of $CuFeSe_2$@PA at different concentrations in an EP tube. The NIR laser was produced using an 808 nm high-power multimode pump laser. Temperature changes and thermal images of the irradiated aqueous dispersions were monitored using an infrared thermal imaging instrument.

Dispersion solution of $CuFeSe_2$@PA at various concentrations (0, 0.125, 0.25, 0.5, and 1 mg/mL) were continuously irradiated with an 808 nm NIR laser at a power density of 1.5 W/cm$^2$ for 5 min, with PBS solution serving as a control. An IR thermal imager recorded photothermal images and temperature variations in all samples. Photothermal conversion cycling-heating of $CuFeSe_2$@PA was also conducted under 808 nm laser irradiation at 1.5 W/cm$^2$ for five on/off cycles, with data acquired using an IR camera.

## Photothermal Conversion Efficiency of $CuFeSe_2$@PA

The photothermal conversion efficiency (η) of $CuFeSe_2$@PA in aqueous solution was calculated according to the reference.[12] Briefly, 1 mg/mL $CuFeSe_2$@PA solution was exposed to an 808 nm laser (1.5 W/cm$^2$, 15 min) until it reached a steady-state temperature and then cooled down for 20 min. Pure water was used as a negative control. The temperature was recorded during the whole heating-cooling process. Photothermal conversion efficiency (η) was measured according to the following equation:

$$\eta = \frac{hs(T_{max} - T_{surr}) - Q_0}{I\left(1 - 10^{-A_{808}}\right)} \tag{1}$$

In the equation (1), $h$ refers to the heat transfer coefficient; $s$ refers to the surface area of the container; $T_{max}$ and $T_{surr}$ are the maximum temperature and ambient temperature, respectively, to which the sample rises after 15 minutes of irradiation; the $Q_0$ represents is the heat absorbed by the water when the cuvette contains the same volume; $I$ is the laser power and $A_{808}$ is the absorbance at 808 nm. In addition, $hs$ in this equation need to be calculated as follows:

$$hs = \frac{m_d C_d}{\tau_s} \tag{2}$$

In the equation (2), md is the mass of the solution containing the photoactive material; $C_d$ is the specific heat capacity of the water and $\tau_s$ is the associated time constant and calculated by the following equation:

$$\tau_s = \frac{t}{-ln\theta} \tag{3}$$

In the equation (3), $\theta$ is known as the driving force temperature, and it needs to be calculated as follows:

$$\theta = \frac{T - T_{surr}}{T_{max} - T_{surr}} \tag{4}$$

## PTT of $CuFeSe_2$@PA Towards Cancer Cells

4T1 cells were seeded for 24 h in confocal dishes (Nest) with a diameter of 14 mm, followed by treatment with $CuFeSe_2$@PA at a concentration of 100 μg/mL for 24 h, and then irradiated with a laser (808 nm, 1.5 W/cm$^2$, 10 min). The control groups were not treated, either laser irradiation, or incubation of $CuFeSe_2$@PA. The fluorescence images were analyzed by wide-field inverted fluorescence microscope (Leica DMi8, Germany) using a Calcein AM channel with an excitation band of 460 nm-500 nm and an emission band of 512–542 nm, PI channel with an excitation band of 532 nm-558 nm and an emission band of 570–640 nm.

## MR and CT Performance In vitro and In vivo

$T_2$-weighted imaging was conducted using Siemens Prisma 3.0T magnetic resonance equipment, with simultaneous measurement of the $T_2$ signal intensity for each concentrated solution. The MRI scanning parameters were set as follows: TE time 70 ms, TR time 3000 ms, FOV 30×60×25 mm, layer thickness 1.0 mm, layer spacing 0.15 mm, matrix 256×256, and measuring area 20 mm$^2$. For in vivo MR scans of the animal model, cross-sectional tumor sites were selected after the completion of scans. The region of interest (ROI) was delineated, and changes in the $T_2$ value were measured, with a measurement area of 5 mm$^2$. CT imaging scans were performed using a Philips IQon CT (PHILIPS, Holland), and the CT value of each concentrated solution was measured. CT scanning parameters were set as follows: 120 KV, 100 mAs, 40 keV, FOV=150 mm, 512×512 matrix, layer

thickness = 0.14 mm, measuring window width 200, window position 80, measuring area 13.49 $mm^2$. Following the CT scan of experimental animals, the ROI of the tumor site was sketched, and CT values were measured. The measurement window width was 350 mm, the window position was 60 mm, and the measurement area was 5 $mm^2$.

## Cytotoxicity Assays and In vitro Targeting Evaluation

To assess the toxicity of $CuFeSe_2$@P and $CuFeSe_2$@PA to MCF-10A cells and 4T1 cells, a cell counting kit (CCK-8) was employed. MCF-10A and 4T1 cells, obtained from the American Type Culture Collection (ATCC), were cultured at the Clinical Experiment Center of the Affiliated Hospital of Southwest Medical University. MCF-10A cells were cultured using DMEM complete medium, and 4T1 cells were cultured using RPMI-1640 complete medium in an incubator at 37 °C and 5% $CO_2$. MCF-10A cells and 4T1 cells were seeded into 96-well plates ($1\times10^6$ cells/well) and incubated for 24 h. Subsequently, various concentrations of $CuFeSe_2$@PA (0, 10, 20, 40, 60, 80, and 100 μg/mL) were added and incubated with cells for 24 h. The CCK8 method was then employed to assess the cell survival rate.

## In vitro Targeting Evaluation

In order to visualize the targeting of $CuFeSe_2$@PA, MCF-10A and 4T1 cells ($1\times10^4$/mL, 300uL) were incubated into confocal culture dishes for 48 hrs, and treated with PBS, $CuFeSe_2$@P-Cy5.5, and $CuFeSe_2$@PA-Cy5.5 for 6 h, respectively. Under an inverted fluorescence microscope, the luminescence of the cells was observed, and the excitation channel was set as Y5, the magnification was 1000 times, and the exposure time was 100 ms. To investigate the source of the targeting ability, MCF-10A cells and 4T1 cells were incubated with free AMD3100 for 1 h, respectively, prior to treatment with $CuFeSe_2$@PA-Cy5.5.

## Tumor Model

All animal experiment protocols were approved by the Laboratory Animal Welfare and Ethics Committee of Southwest Medical University (Number: 20210811–25) to ensure compliance with the National Standards of the People's Republic of China (GB/T35892–2018) Laboratory animal-Guideline for ethical review of animal welfare. Animal procedures involving BALB/c nude mice (Sipeifu, Beijing), weighing 15–22 g, females aged 6–8 weeks, were performed in accordance with institutional animal regulations outlined in the National Institutes of Health Guide for the Care and Use of Laboratory Animals (NIH Publications No. 8023, revised 1978)). To obtain tumor-bearing mice, 4T1 cells ($2\times10^6$) were administered to the backs of the mice. When the tumor size reached approximately 100 $mm^3$, all tumor models of 4T1 tumor-bearing mice were established.

## In vivo Cancer Treatment

A 4T1 xenograft tumor model was established by injecting 4T1 cells into the subcutaneous tissues of BALB/c nude mice. Once the tumor reached a diameter of approximately 0.5 cm, mice-bearing tumors were injected with $CuFeSe_2$@PA at a dose of 50 mg/kg of mice weight and irradiated with an 808 nm laser for 10 min at a power of 1.5 W/$cm^2$. Meanwhile, four experimental groups were used to assess therapy efficiency: (a) tail intravenous injection of 200 μL PBS; (b) tail intravenous injection of 200 μL PBS and irradiation; (c) intratumor injection of $CuFeSe_2$@PA and irradiation, and (d) tail intravenous injection of $CuFeSe_2$@PA. The weights and tumor sizes of the mice were monitored throughout the treatment period. Tumor volumes were calculated using the equation: $Vtumor = (a \times b^2)/2$ (a and b represent the maximum and minimum tumor diameters, tumor). Relative tumor volumes were calculated as V/Vo (V and Vo represent the tumor volume after treatment and the initial tumor volume). Post treatment, hematoxylin and eosin (H&E) staining was performed on the heart, liver, spleen, lungs, kidneys, and other major organs of the mice and cell morphology was observed under optical microscope.

## Statistical Analyses

All statistical data are expressed as the mean ± standard deviation (SD) as indicated. Differences among multiple groups were determined by one-way analysis of variance (ANOVA). A p-value of $<0.05$ was selected to indicate statistical significance, and the data were classified according to their p-values and denoted by *p $<0.05$ and **p $<0.01$; "ns" indicates no statistical significance with $p > 0.05$.

# Results and Discussion

## Characterization of the $CuFeSe_2$@PA Composite

$CuFeSe_2$ nanoparticles, known for their desirable functions and ease of synthesis, were extensively studied.[12–14] To ensure in vivo evaluation and application under mild conditions, $CuFeSe_2$ nanoparticles underwent modifications through dopamine polymerization to enhance their biocompatibility and stability.[27] Subsequently, AMD3100 was introduced onto the surface to improve the active targeting ability of $CuFeSe_2$@PA. The morphology of the $CuFeSe_2$@PA was examined using TEM. As shown in Figure 1a and S3, $CuFeSe_2$@PA exhibited stacked clusters with regularly round, monodisperse characteristics. The average particle sizes of $CuFeSe_2$ and $CuFeSe_2$@PA were measured by Nano Measurer to be 26.7 ±4.8 and 211.4±32.6 nm, respectively (Figure 1b and c). The typical diffraction angles and crystal face peaks in the XRD patterns of $CuFeSe_2$ and $CuFeSe_2$@PA (Figure 1d) were consistent with the standard cards of $CuFeSe_2$ (JCPDS: 81–1959). After surface modification, the intensity of the $CuFeSe_2$@PA diffraction peak weakened slightly, but the typical crystal structure of $CuFeSe_2$ was maintained. ICP-OES analysis (Figure S4) indicated that the molar ratios of Cu, Fe, and Se in the three nanoplatforms were all approximately 1:1:2, consistent with the theoretical value. These results indicate that the core structure and elemental ratio of $CuFeSe_2$ were well maintained after multiple modifications with various biomacromolecules. In addition, the FTIR analysis of $CuFeSe_2$@P revealed stretching and bending vibration absorption peaks of amino (-$NH_2$) (−3390 $cm^{-1}$, −1510 $cm^{-1}$) and hydroxyl (-OH) (−1289 $cm^{-1}$), confirming successful surface modification of PDA (Figure 1e). Compared with $CuFeSe_2$@P, $CuFeSe_2$@PA exhibited a distinct vibration absorption peak at 750–1250 $cm^{-1}$, consistent with the typical vibration absorption peak at 1000 $cm^{-1}$ for the special macrocycloalkane structure of AMD3100 (Figure 1f). These results demonstrated the successful synthesis of $CuFeSe_2$@PA.

## Photothermal Effect

The in vitro photothermal conversion properties of $CuFeSe_2$@PA were investigated by measuring the temperature changes in solutions irradiated by an NIR laser (808 nm, power density of 1.5 W/$cm^2$) at different concentrations. The infrared thermal images and heating curves indicate that the $CuFeSe_2$@PA solution has excellent photothermal conversion performance in a time- and concentration-dependent manner. After irradiation for 300 s, the highest temperature of $CuFeSe_2$@PA aqueous solution with a concentration of 1 mg/mL reached approximately 56 °C (Figure 2a). Without $CuFeSe_2$@PA, the temperature of PBS barely changed. In addition, increasing the laser power density accelerated and enhanced the photothermal conversion

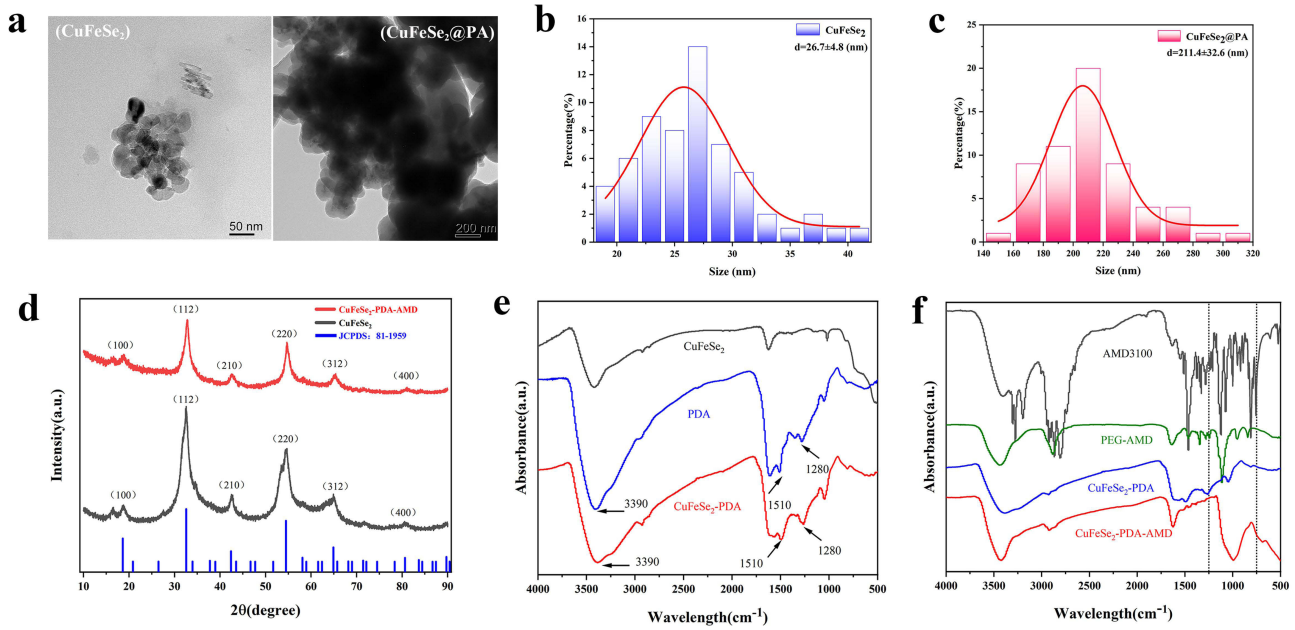


**Figure 1** Characterization of $CuFeSe_2$@PA. (**a**) TEM image of $CuFeSe_2$ and $CuFeSe_2$@PA. (**b**) Particle sizes of $CuFeSe_2$. (**c**) Particle sizes of $CuFeSe_2$@PA. (**d**) XRD image of $CuFeSe_2$ and $CuFeSe_2$@PA. (**e**) FTIR of $CuFeSe_2$, PDA, and $CuFeSe_2$@P. (**f**) FTIR of $CuFeSe_2$@P, $CuFeSe_2$@PA, AMD3100, and PEG-AMD.

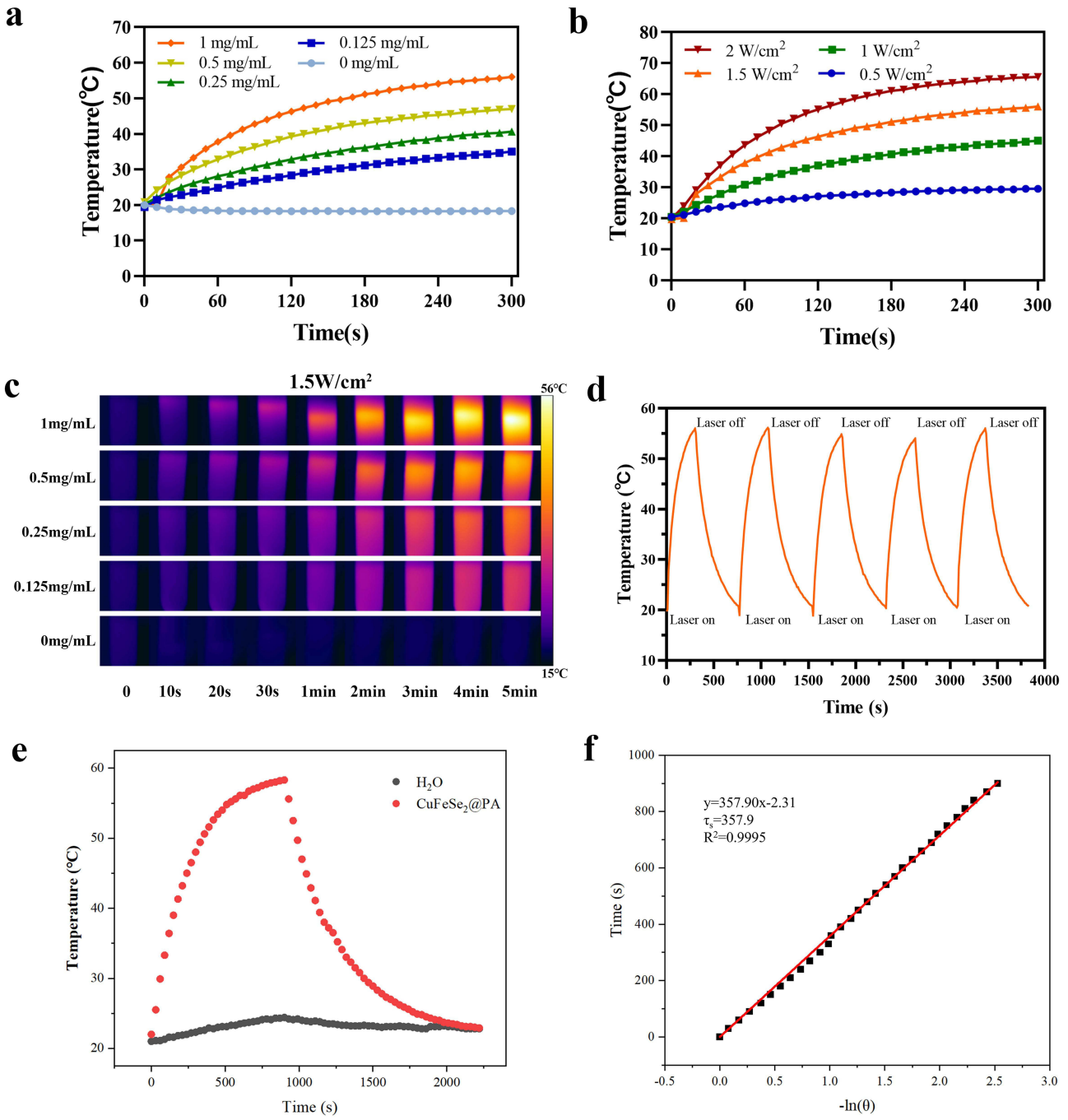


**Figure 2** In vitro photothermal-property characterization of $CuFeSe_2$@PA. (**a**) The change in temperature with time at different concentrations of $CuFeSe_2$@PA irradiated with an 808 nm laser (1.5 W/cm$^2$, 5 min). (**b**) The change in temperature with time of 1 mg/mL $CuFeSe_2$@PA solution by 808 nm laser with different power densities. (**C**) The photothermal images of $CuFeSe_2$@PA at different concentrations under 808 nm laser irradiation at a power of 1.5 W/cm$^2$ for 5 min. (**d**) recycling-heating profiles of $CuFeSe_2$@PA aqueous solution with a concentration of 1 mg/mL after 808 nm laser irradiation at 1.5 W/cm$^2$ for five on/off cycles. (**e**) Temperature profile of $CuFeSe_2$@PA solution (red) and water (black). (**f**) Linear regression of the cooling profile.

of the $CuFeSe_2$@PA aqueous solution (Figure 2b). For practical applications, an NIR laser with a power density of 1.5 W/cm$^2$ was chosen for further experiments, as it could produce sufficient hyperthermia with appropriate energy (Figure 2c). Moreover, under the irradiation of the 808 nm laser, the temperature change of $CuFeSe_2$@PA after five heating and cooling cycles was not obvious, indicating that it had good photothermal stability (Figure 2d). Consequently, the photothermal conversion performance of $CuFeSe_2$@PA NPs was evaluated. $CuFeSe_2$@PA was dispersed in water, and then irradiated with an 808 nm NIR laser at 1.5 W/cm$^2$. As shown in Figure 2e, after irradiation for 900 s, the temperature of $CuFeSe_2$@PA

solution was increased about 36.3 °C. The photothermal conversion efficiency (PCE) was calculated to be 59.2% (Figure 2f). The high photothermal conversion efficiency of CuFeSe2@PA, attributed to its narrow band gap and the introduction of $Fe^{3+}$ ions, enables efficient NIR absorption and heat conversion, outperforming many conventional materials.[12,31] These results demonstrated that $CuFeSe_2$@PA can effectively absorb 808 nm laser energy and generate a substantial amount of superheating, thus ensuring effective in vivo photothermal tumor ablation.

## Biocytotoxicity and Targeting Analysis

Studying the biotoxicity, biocompatibility, and biosafety of $CuFeSe_2$@PA in cells and tissues is important for potential clinical research and applications. To evaluate the biosecurity, we explored the cytotoxicity of $CuFeSe_2$@P and $CuFeSe_2$@PA in normal cells (MCF-10A) and cancer cells (4T1 cells). After $CuFeSe_2$@P and $CuFeSe_2$@PA were co-incubated with MCF-10A and 4T1 cells at high concentrations for 24 h, their viabilities were evaluated the CCK8 method. As shown in Figure 3a and b, even at the highest evaluated concentration of 100 μg/mL, there was no obvious inhibitory effect on MCF-10A and 4T1 cells. In addition, the results of studies on the hemolysis of $CuFeSe_2$@PA in red blood cells have also confirmed its strong biosafety, even with a high concentration of $CuFeSe_2$@PA (up to 5000 μg/mL), the hemolysis level has not been significantly improved (Figure S5). $CuFeSe_2$@PA was intravenously injected into the tail vein of nude mice, and major organs such as the heart, liver, spleen, kidney, and lungs were collected at different time points. H&E staining of these organ sections suggested that no obvious tissue damage occurred (Figure S6). These results indicated that $CuFeSe_2$@PA exhibits good cytocompatibility and biosafety, rendering it suitable for further biological tests. Furthermore, to evaluate the targeting ability of $CuFeSe_2$@PA, $CuFeSe_2$@PA-Cy5.5 and $CuFeSe_2$@P-Cy5.5 were developed by loading the red fluorescent dye, Cy5.5. As illustrated in Figure 3c, when MCF-10A cells were treated with $CuFeSe_2$@PA-Cy5.5 and $CuFeSe_2$@P-Cy5.5, no fluorescence was observed because of the lack of CXCR4 receptors on the surface of normal cells. When $CuFeSe_2$@PA-Cy5.5 and $CuFeSe_2$@P-Cy5.5 were co-incubated with 4T1 cells, only $CuFeSe_2$@PA-Cy5.5 showed strong red fluorescence. Therefore, the uptake of $CuFeSe_2$@PA-Cy5.5 by 4T1 cells was significantly higher than that of $CuFeSe_2$@P-Cy5.5. In addition, when 4T1 cells were pre-treated with free AMD3100, the red fluorescence response was significantly reduced because free AMD3100 competitively inhibited the interaction between $CuFeSe_2$@PA-Cy5.5 and the CXCR4 receptors. These results suggest that $CuFeSe_2$@PA can be selectively taken up by 4T1 cells owing to the targeting properties of the AMD3100 moiety. Subsequently, calcein-AM and PI costaining experiment was performed to study the cellular PTT efficiency of $CuFeSe_2$@PA. As shown in Figure 3d, it can be clearly seen that the control group and the NIR treatment group only have strong green fluorescence (representing living cells), while the $CuFeSe_2$@PA experimental group also has strong green fluorescence and weak red fluorescence (representing dead cells). On the contrary, after laser irradiation, $CuFeSe_2$@PA experimental group showed strong red fluorescence and almost no green fluorescence, indicating that $CuFeSe_2$@PA photothermal treatment has excellent performance.

## In vitro and In vivo MR and CT Properties of $CuFeSe_2$@PA

Given the prominence of Fe as an element in $T_2$-weighted MR, $CuFeSe_2$@PA was investigated as an MR contrast imaging nano agent. As shown in Figure 4a, during the period of 0–1.0 mg/mL, the $T_2$-weighted MR images of $CuFeSe_2$@PA became darker with increasing concentration. The $T_2$ signal intensity was reduced about 5.5 times without and with $CuFeSe_2$@PA (1.0 mg/mL). The longitudinal relaxation ratio (r2) relaxivity of $CuFeSe_2$@PA is linearly fitted and was calculated to be 1.61 $mM^{-1}$ $s^{-1}$ (Figure 4c and S7). Meanwhile, $CuFeSe_2$@PA could also be applied as a CT imaging agent owing to its large amount of Cu. As shown in Figure 4b and d, with an increase in the $CuFeSe_2$@PA concentration, the grey and CT values of the CT image gradually became brighter, and the CT value was positively correlated with the concentration.

Encouraged by the excellent MR and CT imaging performances of $CuFeSe_2$@PA in vitro, we administered $CuFeSe_2$@PA as a dual-model contrast agent to a tumor mouse model to determine its targeted imaging efficacy at different time points. After establishing a subcutaneous 4T1 xenograft tumor model in nude mice, $T_2$-weighted MR and $T_2$-mapping sequence images were recorded before and after the tail intravenous injection of $CuFeSe_2$@PA and $CuFeSe_2$@P. As shown in Figure 5a, b, and S8, after the injection of $CuFeSe_2$@PA (2.5 h), the level of grayness in the tumor area in $T_2$-weighted MR images became significantly darker, indicating a significant decrease in $T_2$ signal intensity (46.28%). Meanwhile, the color of the tumor area in the $T_2$ mapping sequence images changed from red to yellow-green owing to

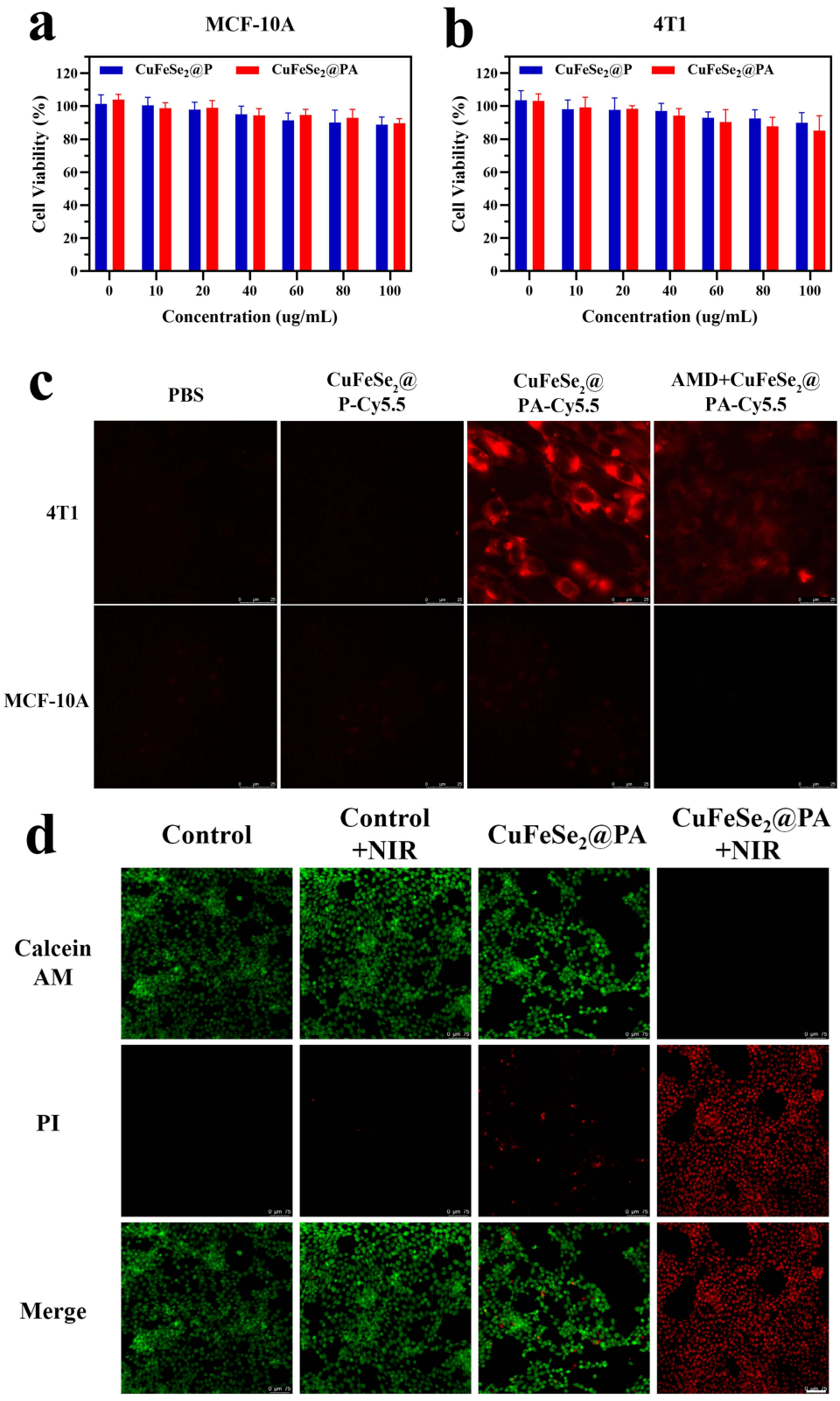


**Figure 3** (**a**) Cell viability of MCF-10A cell incubated with $CuFeSe_2$@P and $CuFeSe_2$@PA for 24 h. (**b**) Cell viability of 4T1 cells incubated with $CuFeSe_2$@P and $CuFeSe_2$@PA for 24 h. (**c**) Fluorescence imaging of 4T1 and MCF-10A cells incubated with PBS, $CuFeSe_2$@P-Cy5.5, $CuFeSe_2$@PA-Cy5.5 for 6 h, and fluorescence imaging of 4T1 and MCF-10A incubated with $CuFeSe_2$@PA-Cy5.5 for 6 h after free AMD3100 pre-treatment for 1 h. Scale bar: 100 μm.(**d**) Fluorescent images of calcein-AM and PI costained 4T1 cells. Scale bar: 75 μm.

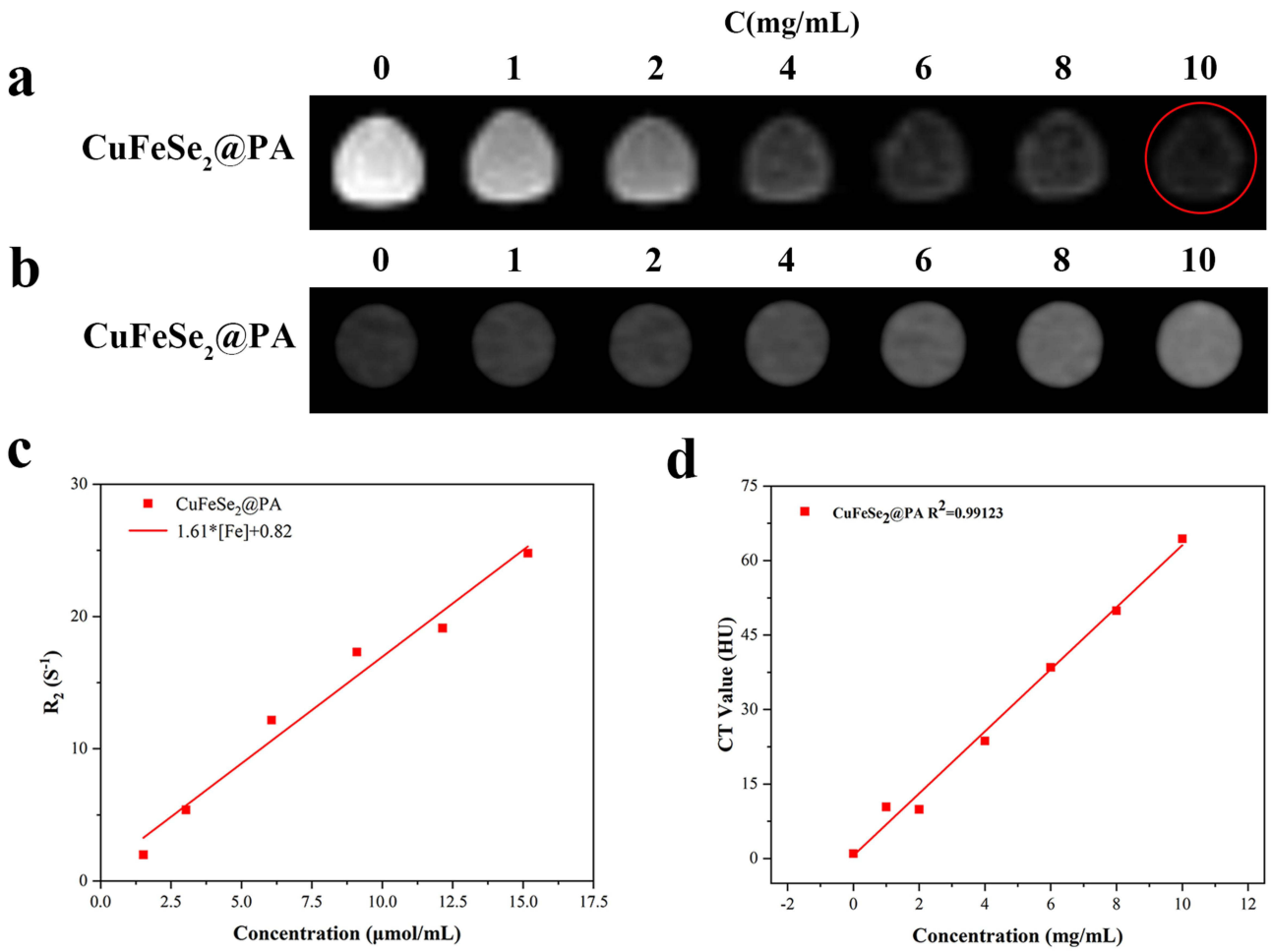


**Figure 4** (**a**) $T_2$-weighted image of $CuFeSe_2$@PA. (**b**) CT image of $CuFeSe_2$@PA. The red circle marks the signal of the solution at 10 mg/mL. (**c**) $T_2$-weighted relaxation rate of $CuFeSe_2$@PA. (**d**) The relationship between CT values and concentration of $CuFeSe_2$@PA.

the significant decrease in $T_2$ values. However, when $CuFeSe_2$@P was treated to 4T1 xenograft nude mice, only a slight change in the $T_2$ signal intensity (decrease of 6.99%) was observed, owing to its non-specific location. Prussian blue staining was performed on the tumor tissues of nude mice injected with $CuFeSe_2$@PA and $CuFeSe_2$@P via the tail vein (Figure S9). The results showed that blue particles representing Fe (red star) appeared only in the tumor tissues of the nude mice treated with $CuFeSe_2$@PA. These results indicate that $CuFeSe_2$@PA has good targeted MR ability in 4T1 xenografted tumor mice. Furthermore, $CuFeSe_2$@PA exhibited a good targeted CT imaging ability. As shown in Figure 5c and S10, the grayness of the tumor areas gradually increased, and the CT values gradually increased within 11 h of the tail intravenous injection of $CuFeSe_2$@PA. These results clearly verified that $CuFeSe_2$@PA is a feasible target contrast agent for tumor-specific MR and CT dual-model imaging.

## In vivo PTT Effect

To evaluate the targeted PTT anti-tumor effect of $CuFeSe_2$@PA, 4T1 tumors-bearing mice were randomly divided into two blank control groups (tail intravenous injection of PBS with and without laser irradiation) and two experimental groups: intratumor injection of $CuFeSe_2$@PA+laser irradiation and tail intravenous injection of $CuFeSe_2$@PA+laser irradiation. After 12 h of administration to the different groups, the mice were subjected to an 808 nm laser (1.5 $W/cm^2$, 10 min) in the tumor region. The temperature changes during laser irradiation were recorded to confirm the NIR PTT effect. Compared with the control group, the temperature of the tumor region in the two experimental groups was significantly higher (Figure 6a and S11). After treatment, the body weight and tumor volume of the tumor-bearing mice

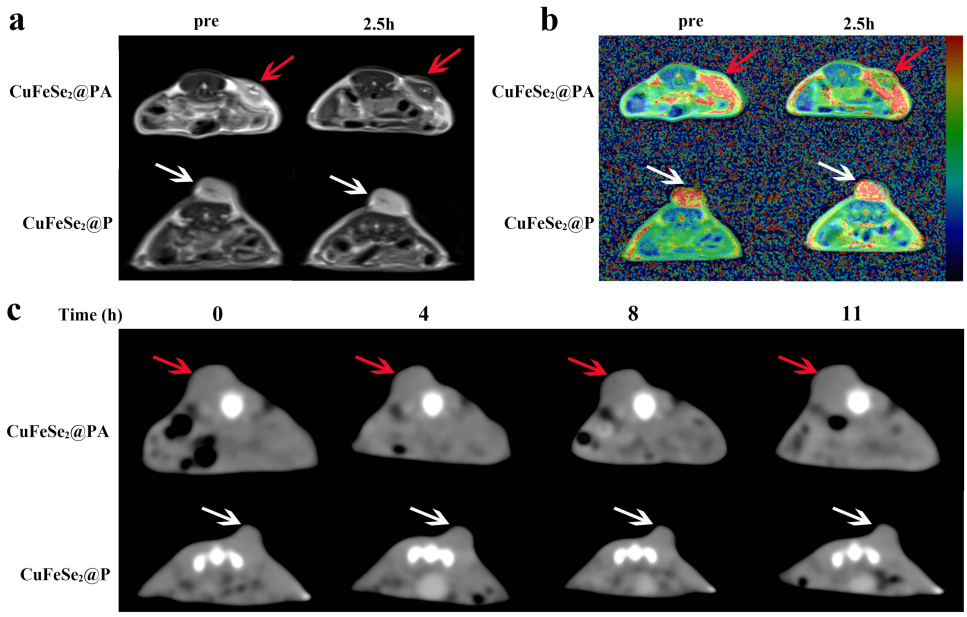


**Figure 5** (**a**) $T_2$-weighted images of 4T1 tumor-bearing nude mice before and after injection of different nano platforms via the tail vein; the red and white arrows show the tumor area. (**b**) Fusion pseudo color images of $T_2$-weighted and $T_2$ mapping sequences of 4T1 tumor-bearing nude mice before and after injection of different nano platforms via the tail vein; the red and white arrows show the tumor area. (**c**) CT images of 4T1 tumor-bearing nude mice before and at different time points after injection of different nano platforms via the tail vein; the red and white arrows show the tumor areas.

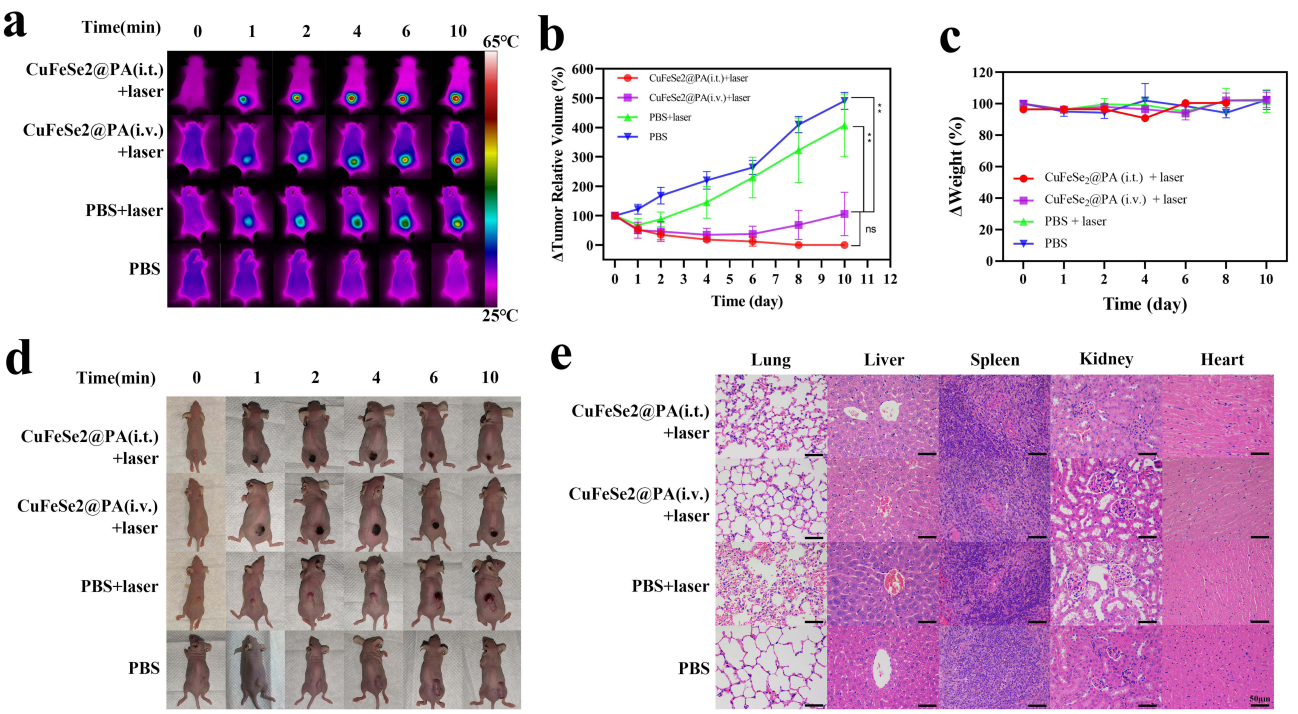


**Figure 6** (**a**) Infrared thermography of nude mice bearing tumor. (**b**) Relative volume changes of tumor in nude mice in each group within 10 days after treatment (one-way analysis of variance was used to assess statistical significance; *p <0.05 and **p <0.01; "ns" indicates no statistical significance with p > 0.05). (**c**) Weight changes of nude mice bearing tumor in each group within 10 days after treatment. (**d**) Photos of nude mice in each group within 10 days after treatment. (**e**) H&E staining images of the heart, liver, spleen, lung, and kidney of nude mice in each group under optical microscope.

were monitored and counted for 10 days (Figure 6b and c). The tumor volumes of the mice in the control group continued to increase. In addition, the tumor growth rate in $CuFeSe_2$@PA-treated experimental groups was almost completely inhibited (Figure 6d). Notably, the intratumor injection group and tail intravenous injection group presented

similar tumor suppression efficiencies owing to the great targeting ability and excellent PTT effects of $CuFeSe_2$@PA. Moreover, the body weights of all mice were maintained at almost the same level during the treatment period, and no inflammation or necrosis was observed in the H&E-stained sections of each organ (Figure 6e), indicating the minimal side effects and good biosafety of $CuFeSe_2$@PA.

## Conclusion

In summary, an "all-in-one" tumor-targeted theranostic platform for targeted photothermal tumor ablation guided by MR and CT dual model imaging based on $CuFeSe_2$ was successfully developed. Owing to the strong interaction between the targeting moiety (AMD3100) and the overexpression of CXCR4 on the membrane of 4T1 cells, $CuFeSe_2$@PA was specifically located in the tumor region of mice bearing 4T1 tumors. This resulted in significant tumor inhibition demonstrated by an excellent PTT effect under 808 nm laser irradiation. Therefore, as a proof-of-concept, $CuFeSe_2$@PA emerges as a promising nanomaterial for targeted clinical cancer theranostics. To ensure the safety and effectiveness of $CuFeSe_2$@PA, additional research will be carried out to further optimize its pharmacokinetics and biocompatibility. Its therapeutic potential may also be increased by broadening the platform's application to target different cancer types with different amounts of CXCR4 expression and by investigating combination therapies with alternative treatment techniques.

## Funding

This work was supported by the National Natural Science Foundation of China (award number: 82272077), and the Key projects of Science and Technology Department of Sichuan Province (award number: 2022YFS0070).

## Disclosure

The authors report no conflicts of interest in this work.

## References

1. Vineis P, Wild CP. Global cancer patterns: causes and prevention[J]. *Lancet*. 2014;383(9916):549–557. doi:10.1016/S0140-6736(13)62224-2
2. Son S, Kim JH, Wang X, et al. Multifunctional sonosensitizers in sonodynamic cancer therapy[J]. *Chem Soc Rev*. 2020;49(11):3244–3261. doi:10.1039/C9CS00648F
3. Wang X, Fan L, Cheng L, et al. Biodegradable nickel disulfide nanozymes with GSH-depleting function for high-efficiency photothermal-catalytic antibacterial therapy[J]. *iScience*. 2020;23(7):101281. doi:10.1016/j.isci.2020.101281
4. Yan P, Shu X, Zhong H, et al. A versatile nanoagent for multimodal imaging-guided photothermal and anti-inflammatory combination cancer therapy[J]. *Biomater Sci*. 2021;9(14):5025–5034. doi:10.1039/D1BM00576F
5. Song G, Kenney M, Chen YS, et al. Carbon-coated FeCo nanoparticles as sensitive magnetic-particle-imaging tracers with photothermal and magnetothermal properties[J]. *Nat Biomed Eng*. 2020;4(3):325–334. doi:10.1038/s41551-019-0506-0
6. Wang H, Mu Q, Revia R, et al. Iron oxide-carbon core-shell nanoparticles for dual-modal imaging-guided photothermal therapy[J]. *J Control Release*. 2018;289:70–78. doi:10.1016/j.jconrel.2018.09.022
7. Oghabian MA, Farahbakhsh NM. Potential use of nanoparticle based contrast agents in MRI: a molecular imaging perspective[J]. *J Biomed Nanotechnol*. 2010;6(3):203–213. doi:10.1166/jbn.2010.1119
8. Chaturvedi VK, Singh A, Singh VK, et al. Cancer nanotechnology: a new revolution for cancer diagnosis and therapy[J]. *Curr Drug Metab*. 2019;20(6):416–429. doi:10.2174/1389200219666180918111528
9. Wozniak M, Ploska A, Siekierzycka A, et al. Molecular imaging and nanotechnology-emerging tools in diagnostics and therapy[J]. *Int J Mol Sci*. 2022;23(5):2658. doi:10.3390/ijms23052658
10. Wang W, Jiang J, Ding T, et al. Alternative synthesis of $CuFeSe_2$ nanocrystals with magnetic and photoelectric properties[J]. *ACS Appl Mater Interfaces*. 2015;7(4):2235–2241.
11. Hu B, Zhao Z, Gao X, et al. Se-modified gold nanorods for enhancing the efficiency of photothermal therapy: avoiding the off-target problem induced by biothiols[J]. *J Mater Chem B*. 2021;9(42):8832–8841. doi:10.1039/D1TB01392K
12. Jiang X, Zhang S, Ren F, et al. Ultrasmall magnetic CuFeSe(2) ternary nanocrystals for multimodal imaging guided photothermal therapy of cancer[J]. *ACS Nano*. 2017;11(6):5633–5645. doi:10.1021/acsnano.7b01032
13. Wu M, Fu S, Shu J, et al. Amphiphilic polymer-modified uniform CuFeSe(2) nanoparticles for CT/MR dual-modal imaging[J]. *Contrast Media Mol Imag*. 2020;2020:4891325. doi:10.1155/2020/4891325
14. Yan Y, Yang C, Dai G, et al. Folic acid-conjugated CuFeSe(2) nanoparticles for targeted T2-weighted magnetic resonance imaging and computed tomography of tumors In vivo[J]. *Int J Nanomed*. 2021;16:6429–6440. doi:10.2147/IJN.S320277
15. Liu M, Radu DR, Selopal GS, et al. Stand-alone CuFeSe(2) (Eskebornite) nanosheets for photothermal cancer therapy[J]. *Nanomaterials*. 2021;11(8):2008
16. Yoshimura T, Matsushima K, Tanaka S, et al. Purification of a human monocyte-derived neutrophil chemotactic factor that has peptide sequence similarity to other host defense cytokines[J]. *Proc Natl Acad Sci*. 1987;84(24):9233–9237. doi:10.1073/pnas.84.24.9233

17. Juarez J, Bendall L. SDF-1 and CXCR4 in normal and malignant hematopoiesis[J]. *Histol Histopathol*. 2004;19(1):299–309. doi:10.14670/HH-19.299
18. Domanska UM, Kruizinga RC, Nagengast WB, et al. A review on CXCR4/CXCL12 axis in oncology: no place to hide[J]. *Eur J Cancer*. 2013;49(1):219–230. doi:10.1016/j.ejca.2012.05.005
19. Pozzobon T, Goldoni G, Viola A, et al. CXCR4 signaling in health and disease[J]. *Immunol Lett*. 2016;177:6–15. doi:10.1016/j.imlet.2016.06.006
20. De Clercq E. Mozobil(R) (Plerixafor, AMD3100), 10 years after its approval by the US food and drug administration[J]. *Antivir Chem Chemother*. 2019;27:1630018426. doi:10.1177/2040206619829382
21. Woodard LE, Nimmagadda S. CXCR4-based imaging agents[J]. *J Nucl Med*. 2011;52(11):1665–1669. doi:10.2967/jnumed.111.097733
22. Nimmagadda S, Pullambhatla M, Stone K, et al. Molecular imaging of CXCR4 receptor expression in human cancer xenografts with [64Cu] AMD3100 positron emission tomography[J]. *Cancer Res*. 2010;70(10):3935–3944. doi:10.1158/0008-5472.CAN-09-4396
23. Hartimath SV, Domanska UM, Walenkamp AM, et al. (9)(9)mTc]O(2)-AMD3100 as a SPECT tracer for CXCR4 receptor imaging[J]. *Nucl Med Biol*. 2013;40(4):507–517. doi:10.1016/j.nucmedbio.2013.02.003
24. Miao Y, Zhang H, Cai J, et al. Structure-relaxivity mechanism of an ultrasmall ferrite nanoparticle T(1) MR contrast agent: the impact of dopants controlled crystalline core and surface disordered shell[J]. *Nano Lett*. 2021;21(2):1115–1123. doi:10.1021/acs.nanolett.0c04574
25. Lee H, Rho J, Messersmith PB. Facile conjugation of biomolecules onto surfaces via mussel adhesive protein inspired coatings[J]. *Adv Mater*. 2009;21(4):431–434. doi:10.1002/adma.200801222
26. Ryu JH, Messersmith PB, Lee H. Polydopamine surface chemistry: a decade of discovery. *ACS Appl Mater Interfaces*. 2018;10(9):7523–7540. doi:10.1021/acsami.7b19865
27. Chen T, Liu Z, Zhang K, et al. Mussel-inspired Ag NPs immobilized on melamine sponge for reduction of 4-Nitrophenol, antibacterial applications and its superhydrophobic derivative for oil-water separation. *ACS Appl Mater Interfaces*. 2021;13(42):50539–50551. doi:10.1021/acsami.1c14544
28. Lynge ME, van der Westen R, Postma A, Städler B. Polydopamine–a nature-inspired polymer coating for biomedical science. *Nanoscale*. 2011;3(12):4916–4928. doi:10.1039/c1nr10969c
29. Li B, Gong T, Xu N, et al. Improved stability and photothermal performance of polydopamine-modified Fe3 O4 nanocomposites for highly efficient magnetic resonance imaging-guided photothermal therapy. *Small*. 2020;16(45):e2003969. doi:10.1002/smll.202003969
30. Nicolas-Boluda A, Vaquero J, Laurent G, et al. Photothermal depletion of cancer-associated fibroblasts normalizes tumor stiffness in desmoplastic cholangiocarcinoma[J]. *ACS Nano*. 2020;14(5):5738–5753. doi:10.1021/acsnano.0c00417
31. Li B, Yuan F, He G. Ultrasmall CuCo 2 S4 nanocrystals: all-in-one theragnosis nanoplatform with magnetic Resonance/near-infrared imaging for efficiently photothermal therapy of Tumors. *Adv Funct Mater*. 2017;27(10):1606218. doi:10.1002/adfm.201606218